Numerical analysis of the pore-scale mechanisms controlling the efficiency of immiscible displacement of a pollutant phase by a shear-thinning fluid

Antonio Rodríguez de Castro, Benoît Goyeau

To cite this version:

Antonio Rodríguez de Castro, Benoît Goyeau. Numerical analysis of the pore-scale mechanisms controlling the efficiency of immiscible displacement of a pollutant phase by a shear-thinning fluid. Chemical Engineering Science, 2022, 251, pp.117462. 10.1016/j.ces.2022.117462 . hal-03602406

Numerical analysis of the pore-scale mechanisms controlling the efficiency of immiscible displacement of a pollutant phase by a shear-thinning fluid

Antonio Rodríguez de Castro (1), Benoit Goyeau (2).

(1) I2M, Arts et Métiers Institute of Technology, CNRS, Esplanade des Arts et Métiers, 33405 Talence Cedex, France
(2) Laboratoire EM2C, UPR CNRS 288, Centrale-Supélec, Université Paris-Saclay. 3 rue Joliot-Curie, 91190 Gif-sur-Yvette.

*Corresponding author
Dr. Antonio Rodríguez de Castro
Arts et Métiers ParisTech
Rue Saint-Dominique
51006 Châlons-en-Champagne
France
Tel: +33 326699173
Email: antonio.rodriguezdecastro@ensam.eu

Abstract

Knowledge of the pore-scale physics of underground multiphase flows is essential to devise efficient soil remediation methods. However, the immiscible displacement of pollutant through the injection of a shear-thinning fluid remains poorly understood. The current work presents a full set of direct numerical simulations in which a Newtonian contaminant is displaced by a Carreau fluid or, alternatively, by a Newtonian fluid, in three porous media with different degrees of microstructural complexity. Imbibition, drainage and neutral wettability cases are considered, and the sensitivity of residual pollutant saturation to Carreau's law parameters is also assessed. The present results allow for the quantification of the performance of immiscible displacement using shear-thinning invading fluids. This performance is shown to depend on the value of capillary number and the heterogeneity of the porous microstructure, which determine the relative importance of viscous fingering, capillary forces and pollutant trapping behind the invasion front.

Keywords: Shear-thinning fluids; Multiphase flow; Pore-scale numerical simulations; Shear viscosity distribution; Solid-fluid interactions.

1. Introduction

Multiphase flows in porous media are widely investigated because of their relevance in soil remediation processes (Wasan and Nikolov, 2003; Tsakiroglou et al., 2013; Truex et al., 2015), biochemistry (Tassi, 1996) and tissue biomechanics (Pesavento et al. 2017), among other important areas. In the particular case of underground applications, many organic contaminants have low water solubility and remain trapped in the subsurface as either a separate organic phase liquid (non-aqueous phase liquid NAPL) or separate solid phase. Some examples of light non-aqueous phase liquids are benzene, toluene, xylene and other hydrocarbons (Longpré et al., 2016 ; Forey et al., 2020), while dense non-aqueous phase liquids include mixtures of chlorinated hydrocarbons such as trichloroethene, tetrachloroethene or perchloroethylene (Hirasaki et al., 1997; Smith et al., 2008). Where they are present, separate phase or sorbed pollutants serve as a long-lived contamination source to groundwater (National Research Council, 2005).

Non-Newtonian fluids exhibiting shear-thinning behavior, such as foams (Fatin-Rouge and Bertin, 2019, Forey et al., 2020) and polymer solutions (Silva et al., 2012; Zhong et al., 2013), are often used to improve the displacement of pollutants as compared to waterflooding. Indeed, shear-thinning fluids can effectively invade the less permeable strata of heterogeneous media, allowing for their use as mobility control agents in soil remediation processes (Longpré-Girard et al., 2016). In contrast to the simpler case of a Newtonian fluid, the viscosity function for a non-Newtonian fluid depends on shear rate and pore velocity in a complex way. Pores in a natural environment have very variable morphologies, topologies and characteristic lengths. Consequently, the injection of a shear-thinning fluid through a porous medium generates a great diversity of local viscosities (Airiau and Bottaro, 2020). At the Darcy scale, i.e., at the scale where Darcy’s law (or one of its multiple extensions) governing the flow is valid, this results in a non-linear relation between the pressure gradient and the flow rate. For a given porous medium, this nonlinear relationship is commonly established by introducing a characteristic viscosity of the Darcy scale, known as Darcy viscosity μ_D. μ_D is a function of the injection velocity for a shear-thinning fluid, contrairily to the case of a Newtonian fluid (Wu, 1990).

Assuming negligible gravitational forces, immiscible displacement is driven by the competition between capillary and viscous forces at the pore scale (Wilkinson 1984; Lenormand et al., 1988; Akhlaghi Amiri and Hamouda, 2014). The relative influence of these forces can be quantified by means of the capillary number Ca and viscosity ratio M (both being dimensionless):

$$\mathrm{Ca} = \frac{q\,\mu_1}{\sigma} \tag{1}$$

$$\mathrm{M} = \frac{\mu_1}{\mu_2} \tag{2}$$

where q is Darcy velocity, μ_1 and μ_2 are the shear viscosities of the invading fluid and the resident fluid, respectively, and σ is the interfacial tension between both fluids. Favorable displacement corresponds to $M > 1$, and unfavorable to $M < 1$ (Xie et al., 2018). Depending on the values of Ca and M, stable of unstable invasion fronts can be obtained in a given porous medium.

Numerical simulations provide valuable insights into the immiscible displacement mechanisms at the pore scale, which can be complemented by laboratory microfluidic measurements (Rabbani et al., 2017; Konangi et al., 2021). In this respect, some previous studies presented microfluidic experiments in which non-Newtonian fluids were used as displacing fluids (Nilsson et al., 2013; Rodríguez de Castro et al., 2016b). An important conclusion from these works is that recovery efficiency can be improved through the injection of shear-thinning displacing fluids with respect to waterflooding. Furthermore, the dependency of the residual saturation of displaced fluid on Ca was shown to be non-monotonic as a consequence of the changes in the stability of the invading front. Also, experimental visualization studies and theoretical interpretations of the immiscible displacement of shear-thinning-oil phases in homogeneous and heterogeneous pore networks were done in the past. For instance, the gradient percolation approach was coupled with classical macroscopic two-phase flow equations to produce scaling laws for capillary pressure and relative permeabilities, and the models were validated through laboratory experiments (Tsakiroglou, 2005). Moreover, the flow patterns were correlated with shear-thinning rheology in a quantitative basis (Tsakiroglou et al., 2003).

Several commercial and open-source toolboxes exist for modelling multiphase flows in porous media (e.g., Horgue et al., 2015; Helland et al., 2019; Patel et al., 2019; Koch et al. 2021). However, the numerical works dealing with the use of a non-Newtonian displacing fluid are scarce. Apart from the demanding requirements in terms of numerical resources to perform such simulations, the strong nonlinearities arising from the constitutive laws of non-Newtonian fluids also result in a nonlinear relationship between Ca and q (Eq. 1) through an injection-velocity dependent μ_1, which adds a major complication (Rodríguez de Castro et al., 2016b). On this same subject, the work of Amani et al. (2020) reported some significant challenges in the numerical simulation of multiphase flows of non-Newtonian fluids, e.g., accurate tracking of the interfaces, small timestep problems, high Weissenberg number problems with viscoelastic fluids, etc. In the same work, a finite-volume conservative level-set based method was presented allowing for the resolution of this type of multiphase flows. However, porous media applications were not addressed.

Wu et al. (1991) presented an analytical Buckley-Leverett-type solution to describe one-dimensional immiscible displacement of a Newtonian fluid by a power-law fluid in a porous medium, assuming negligible capillary pressure gradients. More recently, Shi and Tang (2016) used a Lattice-Boltzmann method to simulate the immiscible displacement of a power-law fluid by a Newtonian one in a 2D porous medium of extremely high porosity. The effects of Ca, M, Bond number, wettability and power-law exponent on viscous fingering phenomenon were discussed in the preceding work, for both a shear-thinning and a shear-thickening resident fluid. Also, Xie et al. (2018) performed Lattice-Boltzmann simulations at the pore scale to compare the performance of shear-thinning and shear-thickening yield stress fluids as displacing agents under different wetting conditions. The preceding work focused on monitoring the residual saturation of the displaced Newtonian fluids as a function of the cumulative injected fluid volume. In a subsequent work, Wang et al. (2019) also used a Lattice-Boltzmann method to investigate viscous fingering in immiscible displacement in porous media with power-law resident fluids. Their work showed that lower values of n lead to more heterogeneity in the viscosity field of the shear-thinning fluid and result in more stable viscous fingers. These authors chose a high value of injection velocity to ensure that the effects of capillary forces were negligible. Druetta and Picchioni (2020) numerically simulated immiscible displacement of oil by water and non-Newtonian fluids in both a macroscopic 2D cell and a 2D microscopic model, using a level-set method. The preceding work presented a single pore-scale simulation in which the rheology of the displacing fluid was represented by a Carreau model including an elastic-term associated to shear-thickening at high shear rates. Since the authors focused on showing the fundamental role of viscoelasticity in multiphase flows in porous media, the effects of Ca and M on recovery efficiency were not directly addressed.

Although the existing literature provides evidence on the relevance of using shear-thinning fluids to improve sweep efficiency during immiscible displacement of underground pollutants, there is still a lack of detailed investigation into the effects of rheological parameters and injection velocity on the amount of trapped pollutant at breakthrough. Indeed, the range of Ca and the type of fluids and porous media that have been studied is remarkably limited. Consequently, the aim of the present work is to provide a thorough pore-scale investigation of multiphase flows in porous media involving the use of shear-thinning fluids. With this objective in mind, three sets of numerical simulations will be performed in porous media of increasing complexity under different wettability conditions, covering a wide range of injection velocities to ensure significant variations in the relative importance of the different competing mechanisms. Moreover, Carreau fluids with markedly different rheological parameters will be considered in order to elucidate the impact of such parameters on pollutant recovery.

2. Numerical simulations

2.1. Investigated porous media

Multiphase flow was investigated in the three different porous media displayed in Figure 1: a porous medium composed of Aligned Monodisperse Circular solid grains (AMC), a Heterogeneous medium formed by alternating Layers of Circular solid grains of two different sizes (HLC) and a porous medium composed of Disordered Monodisperse Circular solid grains (DMC). The geometry of the DMC medium was obtained from Mehmani and Tchelepi (2017a,b). The porosity and permeability values of the investigated porous media were 0.364 and 3.33×10^{-8} m^2 for the AMC medium, 0.342 and 1.92×10^{-8} m^2 for the HLC medium and 0.390 and 3.33×10^{-10} m^2 for the DMC medium. The permeabilities of the top and the bottom layer of the HLC medium were 5.78×10^{-9} m^2 and 1.78×10^{-8} m^2, respectively. These ranges of porosity and permeability are commonly encountered in soil remediation applications (Fatin-Rouge and Bertin, 2019) and also in the packed beads and structured packings used in chemical engineering (Clavier et al., 2017).

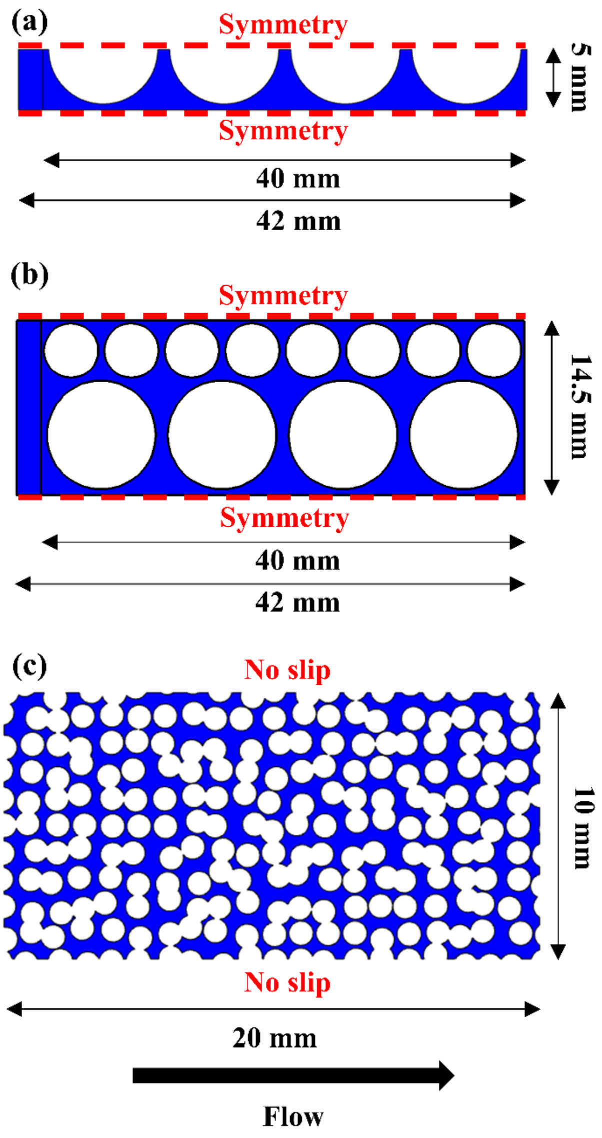

Figure 1. Porous media investigated in the current numerical simulations: (a) Aligned Monodisperse Circular solid grains (AMC medium), (b) Heterogeneous medium formed by alternating Layers of Circular solid grains of two different sizes (HLC) and (c) Disordered Monodisperse Circular solid grains (DMC medium).

2.2. Solved equations and numerical procedure

The flow problems under consideration were solved in the finite element-based simulation software COMSOL Multiphysics version 5.3. (2017). Unstructured meshes composed of triangular element faces were generated to discretize the computational domains, with average element sizes of 141.3 µm for the AMC medium, 407.9 µm for the HLC medium and 79.6 µm for DMC medium. The *Laminar two-phase flow, level set* module, designed for tracking the interface between the immiscible fluids, was used (O'Keefe et al. 2019; Chowdhury et al. 2020). Navier-Stokes equations were solved to take into account mass and momentum conservation:

$$\rho\frac{\partial \mathbf{u}}{\partial t}+\rho(\mathbf{u}\cdot\nabla)\mathbf{u}=\nabla\cdot\left[-p\mathbf{I}+\mu\left(\nabla\mathbf{u}+\nabla\mathbf{u}^{T}\right)\right]+\mathbf{F}_{\sigma} \tag{3}$$

$$\nabla\cdot\mathbf{u}=0 \tag{4}$$

with **u** being the local velocity vector, t being time, μ being the local shear viscosity, **I** being the second-order identity tensor and $\mathbf{F}_{\sigma}$ being the surface tension force acting at the interface between the immiscible fluids. A transport equation for the level set function was solved in order to track the interface position:

$$\frac{\partial\varphi}{\partial t}+\mathbf{u}\cdot\nabla\varphi=\zeta\nabla\cdot\left(\varepsilon\nabla\varphi-\varphi(1-\varphi)\frac{\nabla\varphi}{|\nabla\varphi|}\right) \tag{5}$$

with φ being the level set function, ζ being the reinitialization parameter and ε being the parameter controlling the thickness of the interface. φ is a smooth function that equals zero within the resident phase domain, one within the displacing fluid domain and intermediate values at the interface between both fluids. Hereafter, it will be considered that the interface is defined by the $\varphi = 0.5$ isocontour.

Numerical instabilities may lead to oscillations in φ if the value of ζ is too small, while the movement of the interface will not be correctly reproduced if the value of ζ is too high (Chowdhury et al., 2019). ζ was taken as being of the same order of magnitude as the maximum velocity of the interface between displacing and displaced fluids in all the current simulations (Han and Chen, 2019; Cadiau et al., 2020), i.e., either u or 10 × u, depending on the boundary conditions. The default value of ε taken by COMSOL was used, which corresponded to half the maximum element size in the mesh (Olsson and Kreiss, 2005; Chowdhury et al., 2020; Santos et al., 2020): ε = 90.4 μm for the AMC medium, ε = 282.6 μm for the HLC medium and ε = 74.7 μm for the DMC medium.

Density and dynamic viscosity are a function of φ and are defined as follows:

$$\rho = \rho_1 + (\rho_2 - \rho_1)\varphi \quad (6)$$

$$\mu = \mu_1 + (\mu_2 - \mu_1)\varphi \quad (7)$$

where subscripts 1 and 2 refer to the injected and the displaced fluid, respectively.

A generalized shear rate $\dot{\gamma}$ can be defined by using Einstein's summation convention: $\dot{\gamma} = \sqrt{2\Delta_{i,j}\Delta_{i,j}}$ with $\Delta_{i,j} = \frac{1}{2}\left(\frac{\partial \mathbf{u}_i}{\partial x_j} + \frac{\partial \mathbf{u}_j}{\partial x_i}\right)$ and (x_i, x_j) being the spatial coordinates. Carreau model was implemented to quantify the local viscosity of the shear-thinning fluid:

$$\mu_2 = \mu_\infty + (\mu_0 - \mu_\infty)[1 + (\lambda\dot{\gamma})^2]^{\frac{n-1}{2}} \tag{8}$$

Symmetry boundary conditions were imposed in the lateral walls of the AMC and HLC media, prescribing no penetration ($\mathbf{u} \cdot \mathbf{n}_{\mathrm{wall}} = 0$, with $\mathbf{n}_{\mathrm{wall}}$ being the unit vector normal to the boundary) and vanishing shear stresses ($\mathbf{S} - (\mathbf{S} \cdot \mathbf{n}_{\mathrm{wall}})\mathbf{n}_{\mathrm{wall}} = 0$ with $\mathbf{S} = \mu\left(\nabla\mathbf{u} + \nabla\mathbf{u}^{\mathrm{T}}\right)\mathbf{n}_{\mathrm{wall}}$)). However, no slip conditions were used for the DMC medium so as to mimic flow through a microfluidic device. The main flow direction was from the left to the right as shown in Figure 1. A constant horizontal injection velocity u was imposed at the inlet of the media (left boundary) and the outlet pressure was kept equal to 0 Pa (right boundary). A wetted surface boundary condition was imposed at the external surface of the solid grains (Chowdhury et al. 2020), which enforces no-penetration ($\mathbf{u} \cdot \mathbf{n}_{\mathrm{wall}} = 0$) and adds a frictional force on the form $\mathbf{F}_{\mathrm{frictional}} = -\frac{\mu}{\beta}\mathbf{u}$. β is the slip length, and was taken as being equal to the mesh element size (Renardi et al. 2001; Dai et al. 2017; O'Keefe et al. 2019). The wetted surface boundary condition imposes that the extrapolated tangential velocity component is equal to zero at a distance β from the wall.

Different values of u, μ_0, λ, n and contact angle θ were imposed depending on the considered numerical experiment, and the resulting distributions of the displacing and displaces phases were computed over time until breakthrough of the invading front, together with the corresponding shear viscosity and velocity distributions. The non-linear system of equations was solved using the fully coupled approach of the COMSOL *Time Dependent Solver*. Newton-Raphson method were used to seek the solution, taking an initial guess as initial values of the dependent variables. Within each Newton-Raphson iteration, the resulting system of linearized equations was solved using the direct solver PARDISO (Schenk and Gärtner,2004). The solution was considered converged upon reaching a residual below the default physics-controlled relative tolerance (0.01) suggested by COMSOL (Gunde et al., 2010; Stute et al., 2013; Orgogozo et al., 2013; Papatzakos, 2016). A backward differentiation formula was used as time-stepping scheme, and the absolute tolerance setting of the time dependent solver was defined by scaling down the relative tolerance by a factor of 0.05. Mesh grid refinement studies were conducted for most configurations. To do so, the same case was simulated with finer meshes than the one initially selected. By following this procedure, no significant variation in the results was observed, ensuring the accuracy of the solution.

A Newtonian resident fluid with viscosity $\mu = 10$ Pa s was considered in all the current numerical experiments. This value of μ is representative of high viscosity crude oils, natural bitumen and extra-heavy oils (World Energy Council, 2010). The displacing fluid exhibited either Newtonian or Carreau behavior depending on the considered case. A value of $\mu_\infty = 0.001$ Pa s was chosen for all the Carreau displacing fluids. The type of displacing fluids and the values of θ and u studied for each porous medium are summarized in Table 1. More details on the conditions used in each experiment are provided in the supplementary material section (Tables S1 to S4). The values of the Carreau parameters were selected based on auxiliary rheological measurements performed on concentrated xanthan gum solutions by using a shear-stress imposed rheometer equipped with a cone-plate geometry as well as on the results of other researchers (e.g., López, 2004).

Porous medium	θ (º)	Range of u (m/s)	Displacing fluids	Tables
AMC	(30º, 90º, 150º)	(0.0001, 0.0005, 0.001, 0.005, 0.01)	1 Newtonian and different Carreau fluids	S1 and S2
HLC	30º	0.01	Different Newtonian and Carreau fluids	S3
DMC	(30º, 90º, 150º)	(0.0001, 0.001, 0.005, 0.01)	Different Carreau fluids	S4

Table 1. Experimental conditions: range of contact angle θ, injection velocity u and fluids.

It should be noted that the value of q used in Eq. (1) for the determination of Ca was calculated as the line integration over the inlet of the considered medium of the velocity component in the main flow direction divided by the width of the medium (its vertical size). For the calculation of M and Ca (Eqs. 1 and 2), μ_1 was considered as being the surface average shear viscosity in the areas filled with displacing fluid at breakthrough time (regions with $\varphi < 0.5$). These definitions of Ca and M are consistent with the ones used in the few available works addressing the numerical simulation of immiscible displacement in porous media in the presence of a non-Newtonian displacing fluid (e.g., Shende et al., 2021a;b).

3. Results

3.1. Porous medium composed of aligned monodisperse circular solid grains

3.1.1. Effects of wettability on residual pollutant saturation under different capillary numbers

In Figure 2, S_{ro} is represented as a function of u for the simulations performed on the AMC medium under different wettability conditions for the Newtonian and the non-Newtonian displacing fluids. First of all, it can be observed that S_{ro} is a monotonically increasing function of u in this medium, for both fluids and for all values of θ. This is in contrast to the results of Larson et al. (1977), who predicted, on the basis of percolation theory, a nearly constant S_{ro} under low Ca followed by a monotonic decrease in S_{ro} as Ca increased. However, the preceding work assumed that S_{ro} was only affected by the size of the largest ganglion of resident phase not being mobilized during viscous flow of the displacing fluid, which decreased with u. Subsequent works proved that residual phase distribution was influenced by both Ca and M (Joekar-Niasar and e, 2012a, 2012b). In this regard, the experimental results of several authors showed that S_{ro} increases with Ca under some flow configurations (Khosravian et al., 2014; Rodríguez de Castro et al., 2015), which is in agreement with the present results.

Moreover, Figure 2 shows that higher values of S_{ro} are obtained at the low injection velocities in the cases of neutral wettability (Figure 2b) and drainage (Figure 2c) as compared to imbibition (Figure 2a). This applies to both the Newtonian and the Carreau displacing fluids (18.45 % increase in S_{ro} for $\theta = 150^{\circ}$ as compared to $\theta = 30^{\circ}$ at $u = 0.0001$ m/s for the Newtonian displacing fluid and 5.58 % for the Carreau fluid). Also, the observed increase in S_{ro} with u is negligible within the high-u region. A remarkable feature is that, while the differences in terms of S_{ro} obtained with the Carreau and the Newtonian displacing fluids are important at moderate and low values of u for imbibition and neutral wettability, they are practically non-existent in the case of drainage. For example, S_{ro} is 13.79% higher (in absolute terms) at 0.0001 m/s when using a Carreau fluid during imbibition, whereas S_{ro} is only 0.92% higher during drainage.

The differences in terms of S_{ro} observed for the AMC medium, depending on the injection velocity and the shear-rheology of the injected fluid, are related to the extent to which the invading fluid can travel up the interstitial ducts, perpendicularly to the main flow direction. Indeed, most unrecovered pollutant gets trapped in these vertical ducts due to symmetric flow conditions, as can be observed in Figure 3. Given that vertical flow is driven by capillary force, more pollutant is recovered when the value of Ca is low (and therefore at low u). Imbibition with a Carreau fluid with high shear viscosity results in higher values of Ca as compared to displacement by water ($\mu = 0.001$ Pa s) and in the above-mentioned lower recovery rates within the low-u region. Such a comparison between the performances of Carreau and Newtonian fluids is illustrated in Figure 3 for imbibition under different values of u and in Figure 4 for different values of θ at the lowest injection velocity. An interesting remark is the transition observed for Newtonian imbibition from Figure 3(g), in which the displacing fluid can travel up the vertical interstices, to Figure 3(i), in which pollutant is almost exclusively recovered from the horizontal ducts. This feature explains the significant increase in S_{ro} reported in Figure 2(a) at the intermediate values of u.

Examples of the local shear viscosity distributions of the displacing fluid provided by the current numerical simulations are provided in the supplementary material of this article (Figure S1). As expected, a decrease in viscosity values is observed as u is increased, due to shear-thinning behavior. Moreover, most local viscosity values approach the low shear rates plateau μ_0 at u = 0.0001 m/s. It is reminded that such a limit value is not captured by other simpler non-Newtonian rheological models, such as power-law fluid model. Moreover, Figure S1 shows that the fluid exhibits lower viscosity values in the constrictions of the pores in which it is subjected to higher shear rates.

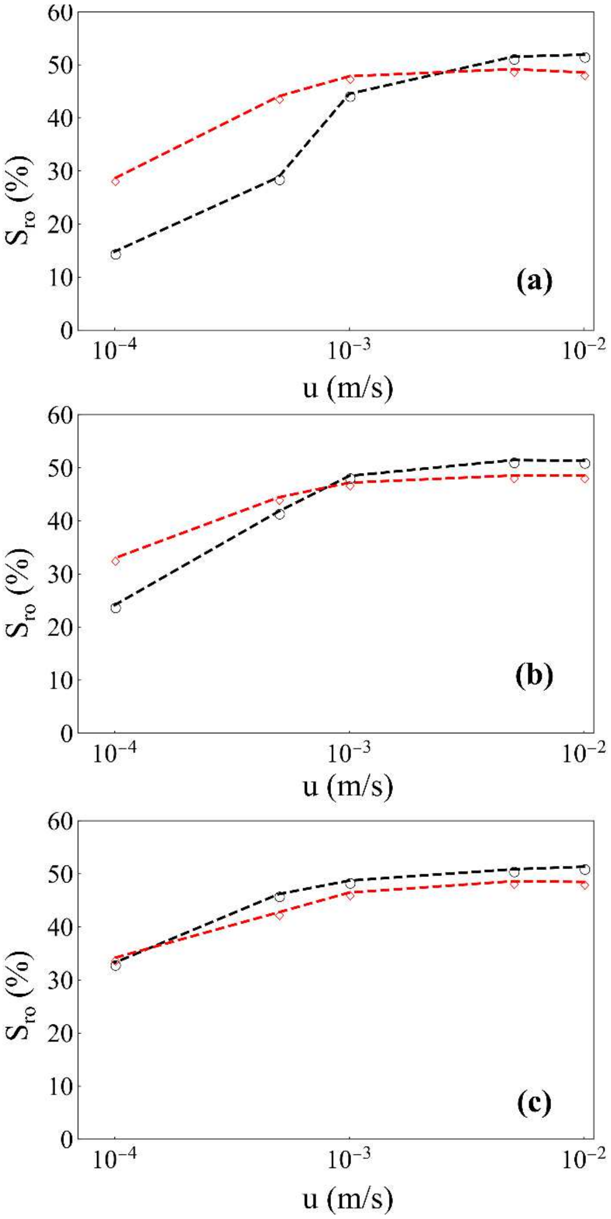

Figure 2. Residual pollutant saturation as a function of injection velocity for (a) imbibition (θ = 30º), (b) neutral wettability (θ = 90º) and (c) drainage (θ = 150º) through the AMC medium. Black symbols joined by black dashed lines correspond to a Newtonian fluid (μ = 0.001 Pa s) and red symbols joined by red dashed lines correspond to a Carreau fluid (μ_0 = 100 Pa s, μ_∞ = 0.001 Pa s, λ = 1 s, n = 0.7).

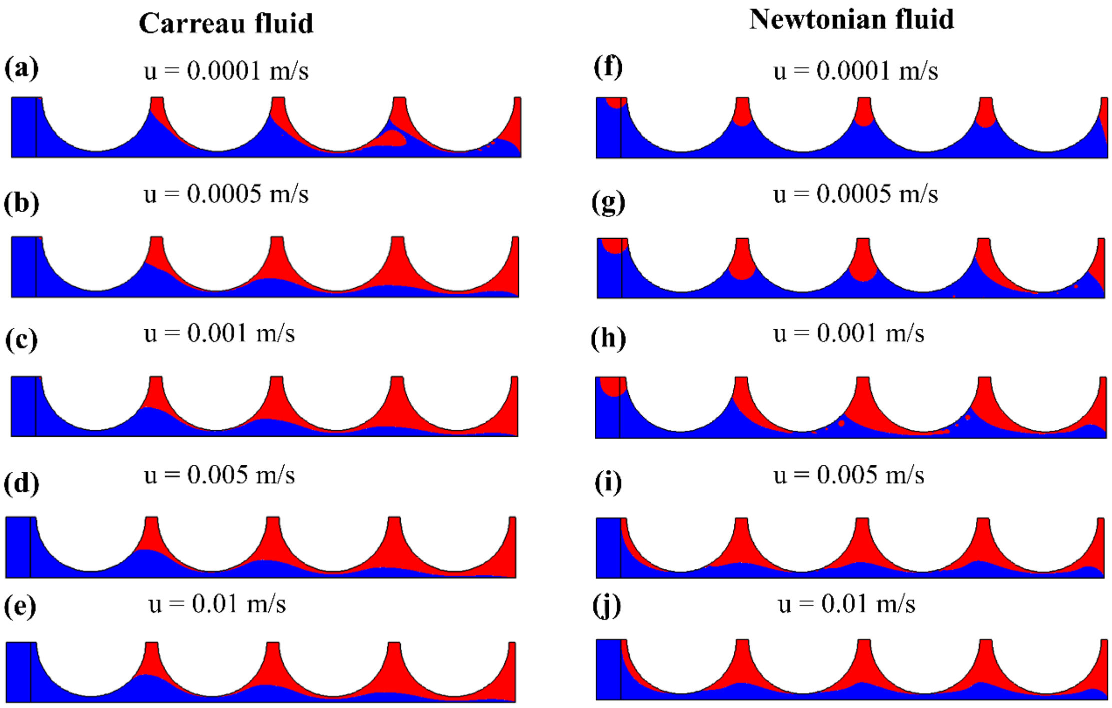

Figure 3. Distribution of the displacing (blue) and displaced (red) phases at breakthrough for imbibition through the AMC medium under different values of u. On the left side of the figure, the case of a Carreau displacing fluid with μ_0 = 100 Pa s, μ_∞ = 0.001 Pa s, λ = 1 s, n = 0.7 is represented. On the right side of the figure, the case of a Newtonian fluid (μ = 0.001 Pa s) is displayed.

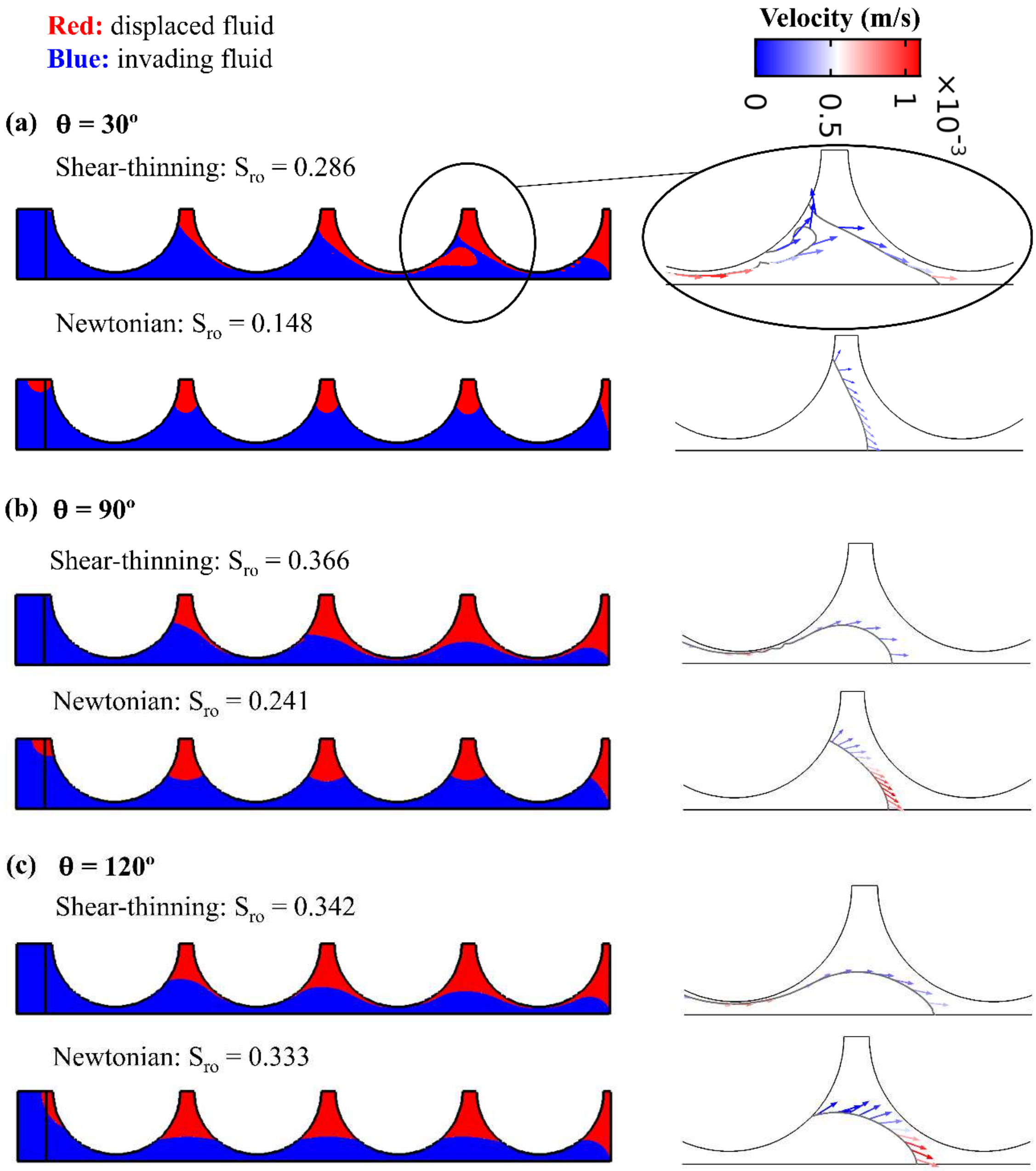

Figure 4. Effects of wettability on residual pollutant saturation at breakthrough at the lowest injection velocity (u = 0.0001 m/s): (a) θ = 30º, (b) θ = 90º and (c) θ = 150º. The left side of the figure shows the distribution of the displacing (blue) and displaced (red) fluids at breakthrough time. The right side of the figure displays the velocity vectors at the interface between both fluids during its flow through the intergranular zone encircled in subfigure (a).

3.1.2. Effects of Carreau's law parameters on residual pollutant saturation during imbibition at low capillary numbers

The results of the imbibition experiments performed on the AMC medium with different Carreau fluids at the lowest injection velocity are displayed in Figure 5. Figure 5(a) shows that

S_{ro} increases when M is increased in the AMC medium. The preceding relationship is well fitted by a logarithmic law, as shown in the same figure. It can be concluded that the use of a Carreau fluid with higher M values than water (Newtonian fluid) is not appropriate for pollutant recovery purposes, which is explained by more resident phase being trapped in the vertical ducts as mentioned above. In this regard, it can be noticed that, if M is increased while keeping u constant, higher values of Ca are obtained (Eqs. 1 and 2). This results in a decrease in the relative importance of capillary forces and less pollutant being displaced from the vertical ducts, without mentioning the higher levels of pressure gradient required to mobilize the fluids.

To go further, the sensitivity of S_{ro} to Carreau's law parameters in the AMC media can also be analyzed from Figure 5(b, c, d) for the lowest value of u (u = 0.0001 m/s). It can be deduced that μ_0 and λ exert a strong impact on pollutant recovery within the investigated range of values, while S_{ro} remains roughly constant independently of the value of n when keeping $\lambda = 1$ s. In other words, shear-thinning behavior is not a determining factor at low injection velocities when dealing with immiscible displacement in regular arrays of identical aligned solids as AMC medium within the investigated range of rheological parameters. This is a consequence of the negligible effect of n on the value of M for this medium. Apart from this, a sharp decrease in S_{ro} is reported for the highest value of λ ($\lambda = 100$ s) in Figure 5(d). This is explained by the low value of $\dot{\gamma}$ marking the onset of shear-thinning behavior in this case ($\dot{\gamma} \sim 0.001$ s^{-1}). This value falls below the average $\dot{\gamma}$ in the medium ($\dot{\gamma} \sim 0.03$ s^{-1}), resulting in a significant decrease in M and improved vertical flow.

All the values of Ca, M, pressure drop, μ_D and S_{ro} obtained at breakthrough time are provided in the supplementary material of this article (Table S1). μ_D was calculated from Darcy's law as:

$$\mu_D = -\frac{K}{q}\nabla P \tag{9}$$

with K being the intrinsic permeability of the porous medium, q being Darcy velocity and ∇P being the pression gradient.

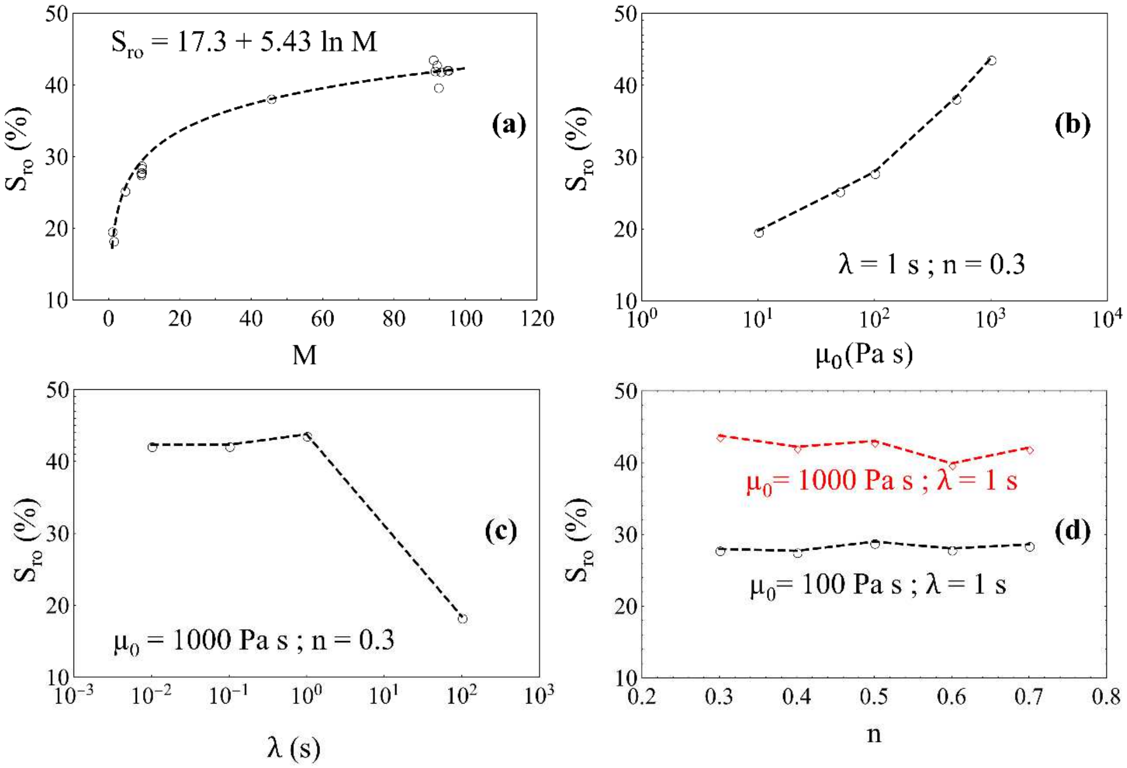

Figure 5. Dependence of S_{ro} on M and on Carreau's model parameters during imbibition at u = 0.0001 m/s in the AMC medium. These results correspond to the injection of the fluids listed in Table S2. (a) S_{ro} vs. M. The average error of the represented fit by a logarithmic law is 3.15 % (b) S_{ro} vs. μ_0. (c) S_{ro} vs. λ. (d) S_{ro} vs. n.

3.2. Heterogeneous medium formed by alternating Layers of Circular solid grains of two different sizes

The residual pollutant saturation in the HLC medium resulting from viscous fingering (Saffman and Taylor, 1958) strongly depends on the shear rheology of the displacing fluid. This is illustrated by the phase distributions displayed in Figure S2 of the supplementary material section. In Figure S2, three examples of rheological parameters leading to high, moderate and low S_{ro} were chosen in order to show the different length of the resulting viscous fingers.

Figure 6(a) shows that S_{ro} is higher at the lowest values of M. These results are consistent with the results of the work of Shi and Tang (2016) for the displacement of a non-Newtonian fluid by a Newtonian one in an extremely porous matrix of staggered squares. Despite the overall trend of the S_{ro} vs. M relationship being increasing, some local fluctuations exist as can be seen in the same figure. This can be explained by the competition between two mechanisms. The first one is the deeper penetration of the invading fluid into the less permeable layer (the top layer in Figure S2) resulting from viscous fingering, which results in important amounts of pollutant not being swept in the low-permeability zone. Viscous fingering becomes less significant as M is increased, because more uniform injection fronts are obtained (as shown in Figure S2). The second mechanism is trapping of pollutant ganglia in the vertical channels between solid grains. This mechanism is illustrated in Figure S3 of the supplementary material section. Figure S3 shows that vertical sweep of pollutant stops once the pollutant is by-passed by two contiguous horizontal fingers of invading fluid, which can occur even under stable front conditions. Given that the amount of pollutant that can be potentially trapped by the second mechanism is low as compared to the first mechanism, the overall trend of S_{ro} vs. M is increasing. However, the second mechanism explains the existence of local fluctuations in Figure 6(a). The value of S_{ro} obtained for water injection (Newtonian fluid) are also displayed for comparison. As can be deduced from the figure, the recovery efficiency was improved through the use of all the tested shear-thinning fluids in the HLC medium.

In order to complete the analysis, the effects of varying the Carreau's parameters of the displacing fluid on recovery efficiency was also investigated. A non-negligible sensitivity of the value S_{ro} to μ_0, λ and n can be deduced from Figure 6(b,c,d). A striking feature of these results is that all the trends reported in Figure 6 for the HLC medium are opposite to those reported in Figure 5 for the AMC medium. Such a difference can be explained by the different relative contributions of capillary pressure-driven flow and viscous fingering to global pollutant recovery in each of these media. While the most efficient method to recover more pollutant from the AMC medium consists in decreasing M while keeping u constant in order to favor vertical flow, as discussed above, this is not the case in the HLC medium, for which low M values favor viscous fingering. All the values of Ca, M, pressure drop, Darcy viscosity and residual pollutant saturations obtained at breakthrough time can be consulted in the supplementary material (Table S5).

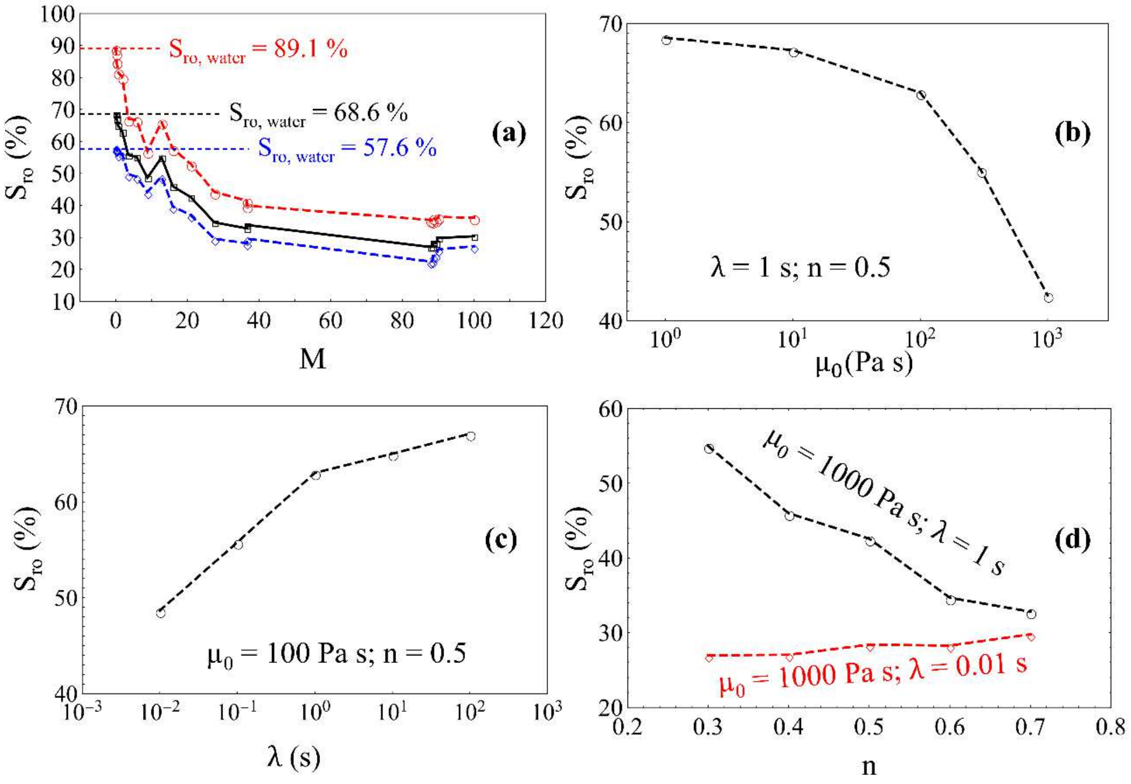

Figure 6. Effects of Carreau's law parameters on residual pollutant saturation during imbibition in the HLC medium at u = 0.01 m/s. (a) S_{ro} as a function of M for the top layer (red color), the bottom layer (blue color) and the whole HLC medium (black color). (b) S_{ro} in the whole HLC medium as a function of μ_0. (c) S_{ro} in the whole HLC medium as a function of λ, (d) S_{ro} in the whole HLC medium as a function of n.

3.3. Porous medium composed of disordered monodisperse circular solid grains

3.3.1. Effects of Carreau's law parameters on residual pollutant saturation at high capillary numbers

In the same manner as for the AMC and the HLC media, the sensitivity of the value of S_{ro} to μ_0, λ and n was also assessed for the DMC medium, and the results are displayed in Figure 7 for imbibition at u = 0.01 m/s. These results are analog to those obtained for the HLC medium, with S_{ro} decreasing when M is increased (in agreement with the results of the work of Shi and Tang, 2016 for the displacement of a non-Newtonian fluid by a Newtonian one in an extremely porous matrix of staggered squares). Furthermore, a local fluctuation in the S_{ro} vs. M relationship is observed at $M \sim 1$ in Figure 7(a), which is analogous to the fluctuations reported in Figure 6(a) arising from the second trapping mechanism mentioned in subsection 3.2. It should be taken into account that the numerical resources required to perform the simulations are more demanding in the case of the DMC medium as compared to the preceding ones, which explains the limited number of data points displayed in Figures 7(b,c,d). However, it seems clear from these figures that the trends of the S_{ro} vs. μ_0, S_{ro} vs. λ and S_{ro} vs. n relationships are similar to those reported in Figure 6 for the HLC medium. It can be deduced from these observations that viscous fingering is the decisive factor contributing to pollutant trapping. Indeed, viscous fingering is progressively suppressed as M is increased, thus improving pollutant recovery. Such an increase in M can be obtained by either a decrease in λ or an increase in μ_0 or n (less pronounced shear-thinning behavior of the injected fluid).

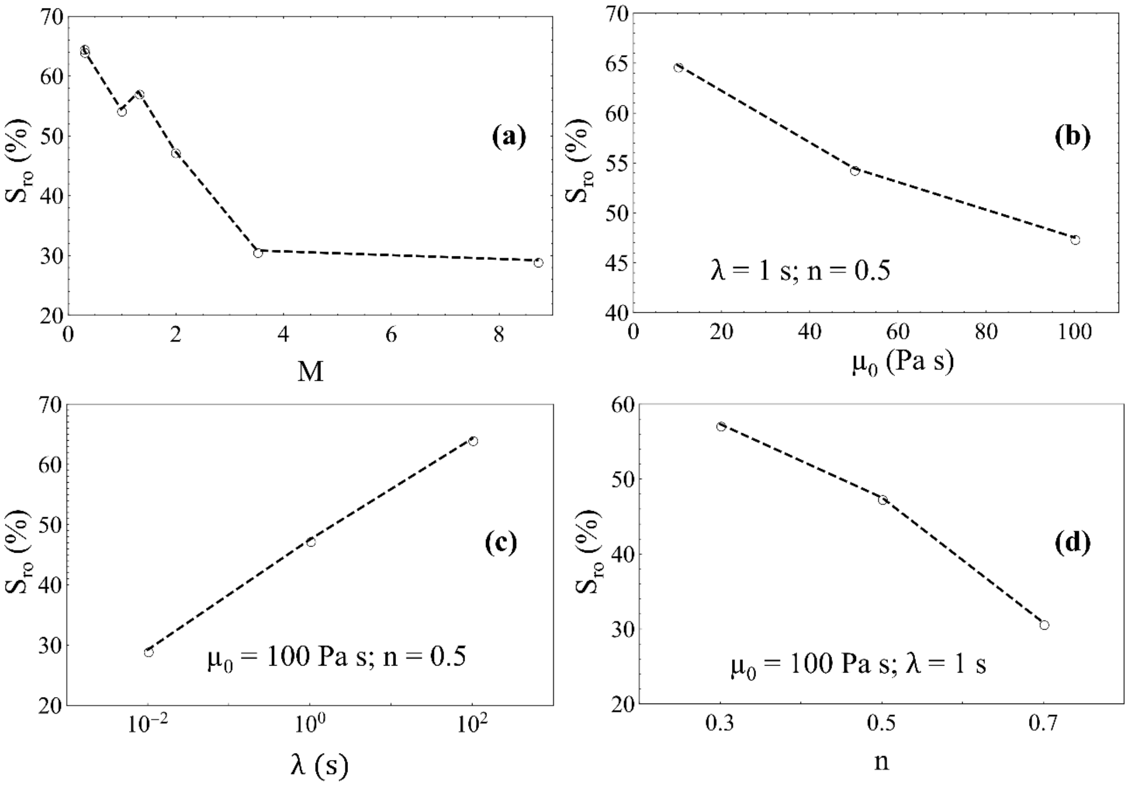

Figure 7. Sensitivity of S_{ro} to M and to Carreau's model parameters during imbibition in DMC medium at u = 0.01 m/s. (a) S_{ro} as a function of M. (b) S_{ro} as a function of μ_0. (c) S_{ro} as a function of λ, (d) S_{ro} as a function of n.

3.3.2. Residual pollutant saturation under different capillary numbers and wettability conditions

The values of S_{ro} at breakthrough time provided by the simulations of the imbibition of a shear-thinning fluid in the DMC medium under different values of Ca are displayed in Figure 8(a). The amount of recovered pollutant decreases as Ca is increased, which is a consequence of the lower values of M obtained at the higher injection velocities (front-destabilizing effect) due to the shear-thinning behavior of the injected fluid (Figures 8(b) and 8(c)). This increase in S_{ro} as Ca increases was also reported in the microfluidic experiments with shear-thinning fluids of Rodríguez de Castro et al. (2016b). Nevertheless, it should be noted that flow through micromodels cannot be considered analogous to the current 2D configurations due to lateral confinement. It should be noted that M is a function of Ca for shear-thinning invading fluids, which is not the case of Newtonian fluids. This means that pollutant displacement by a complex fluid may change from favourable ($M > 1$) to unfavourable ($M < 1$) depending on the value of Ca.

In order to closely investigate how the value of Ca affects the distribution of local viscosities of the shear-thinning fluid during multiphase flow in this porous medium, the shear viscosity maps and histograms are provided in Figure 9. It can be observed that viscous fingering is enhanced as Ca is increased. Moreover, an interesting remark is that the fluid exhibits the upper-limit viscosity μ_0 when injected at low values of Ca. Therefore, using a realistic rheological model is essential to reliably simulate immiscible displacement. However, most of the very few previous works on this topic used a power-law model in which viscosity tends to infinity at the lowest shear rates (e.g., Wu et al. (1991); Shi and Tang (2016) and Xie et al. (2018)). Careful observation of the viscosity maps reveals the fluid exhibits the highest viscosities in the large pore volumes, which is a consequence of the lower values of shear rate in the large pore sections.

The set of three simulations performed at the lowest injection velocity ($u = 0.0001$ m/s), with different wettability conditions ($\theta = 30^\circ$, $\theta = 90^\circ$ and $\theta = 150^\circ$) showed significant differences in terms of recovery efficiency. The obtained values of S_{ro} were 25.9 %, 28.3 % and 32.2 % for imbibition, neutral wettability and drainage, respectively. This proved that a higher amount of pollutant is recovered during imbibition due to the beneficial effect of capillary forces, in agreement with the results of previous works in which Newtonian displacing fluids were used (Akhlaghi Amiri and Hamouda, 2014; Rabbani et al., 2017). All the values of Ca, M, pressure drop, Darcy viscosity and residual pollutant saturations obtained at breakthrough time for the DMC medium are listed in the supplementary material (Table S6).

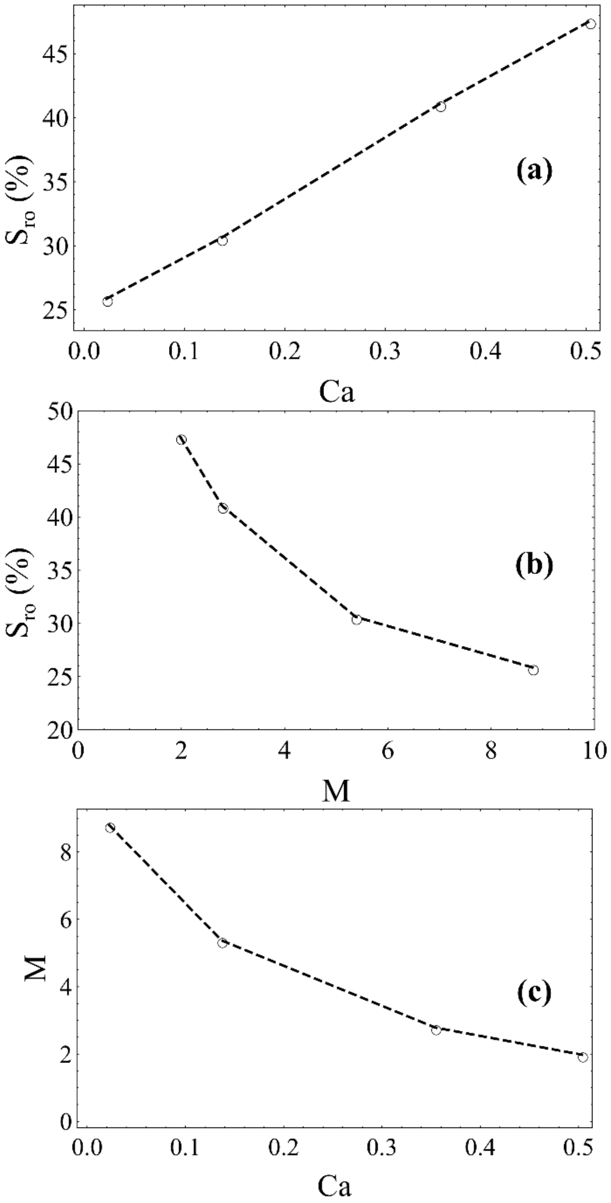

Figure 8. S_{ro} obtained for the imbibition of a Carreau fluid with $\mu_0 = 100$ Pa s, $\lambda = 1$ s, $n = 0.5$ and $\mu_\infty = 0.001$ Pa s through the DMC medium under different values of (a) Ca and (b) M. The dependence of M on Ca is represented in (c).

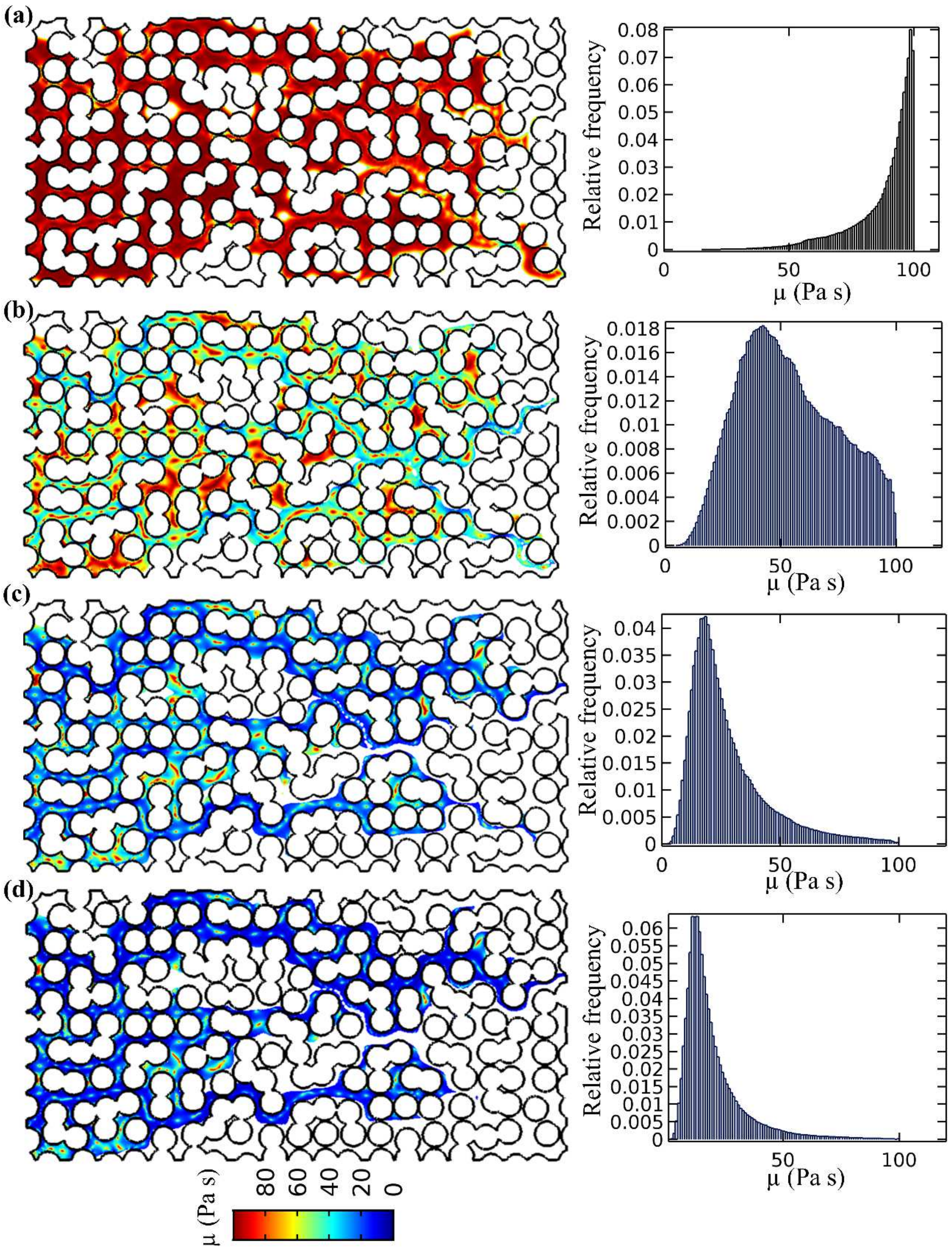

Figure 9. Viscosity of the shear-thinning invading fluid (μ_0 = 100 Pa s, λ = 1 s, n = 0.5 and μ_∞ = 0.001 Pa s) at breakthrough time under different injection velocities: (a) u = 0.0001 m/s, (b) u = 0.001 m/s, (c) u = 0.005 m/s, (d) u = 0.01 m/s). The color map represents the different values of the local shear viscosity of the invading fluid. Resident fluid is represented in white (outside the solid circles). The viscosity histograms are provided on the right side of the figure.

4. Conclusion

A thorough numerical study was conducted using a level-set method in which the immiscible displacement of a viscous pollutant by either a shear-thinning fluid or a Newtonian fluid was considered, assuming negligible buoyancy forces and solid deformation. Three different porous media of increasing complexity (AMC, HLC and DMC) and various Carreau-type displacing fluids were investigated, under different wettability conditions, in order to assess the amount of residual pollutant saturation as a function of Ca and M and shed light on the trapping mechanisms occurring at the pore-scale. The main conclusions of the present simulations can be summarized as follows:

Contrarily to Newtonian fluids, shear-thinning fluids exhibit different shear viscosity values during their flow through a porous medium as a result of the topological and geometrical heterogeneity of the solid microstructure. Such heterogeneity leads to a wide range of local velocities and shear rates, which in turn results in different values of local viscosity as predicted by the non-Newtonian constitutive laws. When the displacing fluid is Newtonian, M is constant and the relationship between Ca and injection velocity is linear. However, this is no longer true when using a non-Newtonian fluid.

More pollutant is recovered under low values of Ca in a matrix of perfectly aligned circles of identical diameter. The reason behind this observation is that pollutant recovery can only be substantially enhanced by favoring flow through the ducts oriented perpendicularly to the main flow direction. This can be achieved through a reduction of the viscosity of the invading fluid, which explains the decrease in S_{ro} when M is decreased. Consequently, the use of a Newtonian invading fluid of low viscosity is more efficient in this type of media. This is particularly true under imbibition and neutral wettability conditions.

The use of shear-thinning fluids exhibiting high viscosity values is recommended when recovering pollutant from heterogeneous media, such as HLC and DMC media. This confirms the experimental results presented in previous works (Silva et al., 2012; Rodríguez de Castro et al., 2016b). In this case, an increased viscosity of the invading fluid produces front stabilization by suppressing viscous fingering. A secondary trapping mechanism has been identified, which consist in the formation of residual pollutant ganglia behind a stable invasion front as a consequence of pollutant being by-passed by invading fluid flowing through adjacent ducts. Also, the inspection of the local shear viscosity maps in DMC demonstrates that using a realistic rheological model such as Carreau equation, which includes a low-shear-rates viscosity plateau, is of vital importance to obtain accurate predictions. It should be noted that polymer flooding is a commonly used chemical enhancement process to displace underground pollutants, since it is simple to apply and requires relatively small investment. The main drawbacks to the use of polymers are their high cost and the low injection rate caused by high viscosity (lower remediation rate) unless high pressures are applied. Other shortcomings include degradation at higher temperatures, intolerance to high salinity and polymer deterioration from shear stress imparted by pumping (Speight, 2016).

This numerical investigation provided an opportunity to understand and quantify the effects of pore-scale mechanisms and fluid-structure interactions that are not readily observable through experimentation. This is of critical importance for the development of innovative solutions enabling us to improve pollutant recovery in underground systems. Moreover, the implementation of the obtained relationships in soil remediation simulation software may increase the accuracy of the predictions made at the pilot plant and the field scales.

Despite these encouraging results, some essential questions are still open. Future works should consider the viscoelasticity (Druetta and Picchioni, 2020) and shear-thickening (Shende et al., 2021c) exhibited by some complex fluids commonly used in soil remediation. Polymer adsorption should also be considered, which can affect permeability and two-phase displacement when the shear-thinning displacing fluids are polymer solutions. However, the importance of polymer adsorption is not always critical in soil remediation operations. For example, xanthan gum biopolymer macromolecules are semi-rigid and are commonly flattened onto the pore wall with negligible modification of the petrophysical characteristics of the porous medium, in contrast to HPAM and other flexible polymers (Chauveteau 1982; Sorbie 1991). This was shown in previous experimental works (Rodríguez de Castro et al., 2016a). Moreover, the present conclusions need to be extended to deforming porous media (Tran and Jha, 2020; Pesavento et al., 2020) and to the case of 3D porous media. 3D capillary forces may be very different from two-dimensional ones, as a consequence of Rayleigh-Plateau instabilities (Romanò et al., 2019;2021), film coating (Fuijoka et al., 2008) and enhanced pore connectivity, among other factors. Also, Chan et al. (2021) recently showed that concave surfaces can localize shear around a liquid bridge’s neck even for a Newtonian fluid, which plays an important role on the stability of liquid films. It is worth bearing in mind that 3D direct numerical simulations of this type of multiphase flow are computationally expensive due, among others, to the strong non-linearities generated by the constitutive equations of complex fluids. Nevertheless, recent advances in pore-network modeling (Joekar-Niasar and Hassanizadeh, 2012c; Sinha et al., 2017; Rodríguez de Castro and Goyeau, 2021) constitute a good starting point to overcome the stumbling block.

5. References

Akhlaghi Amiri, H. A., Hamouda, A. A., 2014. Pore-scale modeling of non-isothermal two phase flow in 2D porous media: Influences of viscosity, capillarity, wettability and heterogeneity. International Journal of Multiphase Flow 61, 14–17.

Amani, A., Balcázar, N., Naseri, A., & Rigola, J., 2019. A numerical approach for non-Newtonian two-phase flows using a conservative level-set method. Chemical Engineering Journal, 123896.

Airiau, Ch., Bottaro, A., 2020. Flow of shear-thinning fluids through porous media. Advances in Water Resources 143, 103658.

Cadiau, S., Courtois, M., Carin, M., Breckmans, W., Le Masson, P., 2020. Heat transfer, fluid flow and electromagnetic model of droplets generation and melt pool behaviour for wire arc additive manufacturing. International Journal of Heat and Mass Transfer 148, 119102.

Chan, S. T., van Berlo, F. P. A., Faizi, H. A., Matsumoto, A., Haward, S. J., Anderson, P. D., Shen, A. Q., 2021. Torsional fracture of viscoelastic liquid bridges. Proceedings of the National Academy of Sciences 118(24).

Chauveteau, G., 1982. Rodlike polymer solution flow through fine pores: influence of pore size on rheological behavior. Journal of Rheology 26, 111–142.

Chowdhury, I. U., Mahapatra, P. S., Sen, A. K., 2019. Self Driven Droplet Transport: Effect of Wettability Gradient and Confinement. Physics of Fluids 31, 042111.

Chowdhury, I. U., Mahapatra, P. S., Sen, A. K., 2020. Shape evolution of drops on surfaces of different wettability gradients. Chemical Engineering Science, 116136.

Clavier, R., Chikhi, N., Fichot, F., Quintard, M., 2017. Modeling of Inertial Multi-Phase Flows through High Permeability Porous Media: Friction Closure Laws, 2017. International Journal of Multiphase Flow 91, 243–261.

COMSOL Multiphysics Version 5.3. COMSOL AB, Stockholm, Sweden. www.comsol.com (2017).

Dai, Y., Zhou, Z., Lin, J., Han, J. (2017). Modeling of Two-Phase Flow in Rough-Walled Fracture Using Level Set Method. Geofluids, 2429796.

Druetta, P., Picchioni, F., 2020. Influence of physical and rheological properties of sweeping fluids on the residual oil saturation at the micro- and macroscale. Journal of Non-Newtonian Fluid Mechanics 286, 104444.

Fatin-Rouge, N, Bertin, H., 2019. Utilisation des mousses pour le traitement des sites et sols pollués - Quelles mousses pour quels usages ? : Principaux acquis et perspectives. [Rapport Technique] ADEME. https://hal.archives-ouvertes.fr/hal-02417471. Accessed 23 Mar. 2021.

Forey, N., Atteia, O., Omari, A., Bertin, H., 2020. Saponin foam for soil remediation: On the use of polymer or solid particles to enhance foam resistance against oil. Journal of Contaminant Hydrology 228, 103560.

Fujioka, H., Takayama, S., Grotberg, J. B., 2008. Unsteady propagation of a liquid plug in a liquid-lined straight tube. Physics of Fluids 20(6), 062104.

Gunde, A. C., Bera, B., Mitra, S. K., 2010. Investigation of water and CO2 (carbon dioxide) flooding using micro-CT (micro-computed tomography) images of Berea sandstone core using finite element simulations. Energy 35, 5209–2521625.

Han, W., Chen, X., 2019. New insights into the pressure during the merged droplet formation in the squeezing time, Chemical Engineering Research and Design 145, 213–225.

Helland, J. O., Pedersen, J., Friis, H. A., Jettestuen, E., 2019. A multiphase level set approach to motion of disconnected fluid ganglia during capillary-dominated three-phase flow in porous media: Numerical validation and applications. Chemical Engineering Science 203, 138–162.

Hirasaki, G.J., Miller, C.A., Szafranski, R., Tanzil, D., Lawson, J.B., Meinardus, H., Jin, M., Londergan, J.T., Jackson, R.E., Pope, G.A., Wade, W.H., 1997. Society of Petroleum Engineers SPE Annual Technical Conference and Exhibition. Proceedings of SPE Annual Technical Conference and Exhibition - Field Demonstration of the Surfactant/Foam Process for Aquifer Remediation.

Horgue, P., Soulaine, C., Franc, J., Guibert, R., Debenest, G., 2015. An open-source toolbox for multiphase flow in porous media. Computer Physics Communications 187, 217–226.

Joekar-Niasar, V., Hassanizadeh S.M, 2012a. Analysis of fundamentals of two-phase flow in porous media using dynamic pore-network models: A review, Critical Rev. Environmental Science & Technology, 42(18), 1895−1976.

Joekar-Niasar, V., Hassanizadeh S.M, 2012b. Uniqueness of specific interfacial area–capillary pressure–saturation relationship under non-equilibrium conditions in two-phase porous media flow, Transport in Porous Media, 94(2), 465–486.

Joekar-Niasar, V., Hassanizadeh S.M., 2012c. Analysis of Fundamentals of Two-Phase Flow in Porous Media Using Dynamic Pore-Network Models: A Review, Critical Reviews in Environmental Science & Technology 42, 1895–1976.

Khosravian, H., Joekar-Niasar, V., Shokri, N., 2014. Effects of flow history on oil entrapment in porous media: An experimental study, AIChE Journal, 61(4), 1385–1390.

Koch, T., Gläser, D., Weishaupt, K., Ackermann, S., Beck, M., Becker, B., Burbulla, S., Class, H., Coltman, E., Emmert, S., Fetzer, T., Grüninger, Ch., Heck, K., Hommel, J., Kurz, Th., Lipp, M., Mohammadi, F., Scherrer, S., Schneider, M., Seitz, G., Stadler, L., Utz, M., Weinhardt, F., Flemisch, B., 2021. DuMux 3 – an open-source simulator for solving flow and transport problems in porous media with a focus on model coupling. Computers & Mathematics with Applications 81, 423–443.

Konangi, S., Palakurthi, N. K., Karamiditriou, N., Comer, K., Ghia, U., 2021. Comparison of pore-scale capillary pressure to macroscale capillary pressure using direct numerical simulations of drainage under dynamic and quasi-static conditions. Advances in Water Resources 147, 103792.

Larson, R. G., L. E. Scriven, and H. T. Davis, 1977. Percolation theory of residual phases in porous media, Nature 268, 409–413.

Lenormand, R., Touboul, E., Zarcone, C., 1988. Numerical models and experiments on immiscible displacements in porous media, Journal of Fluid Mechanics 189, 165–187.

Longpré-Girard, M., Martel, R., Robert, T., Lefebvre, R., Lauzon, J.-M., 2016. 2D sandbox experiments of surfactant foams for mobility control and enhanced LNAPL recovery in layered soils. Journal of Contaminant Hydrology 193, 63–73.

López, X. Pore-scale modelling of non-Newtonian flow, PhD thesis, Dep. Of Earth Sci, Group, Imperial College, London, 2004.

Mehmani, Y., Tchelepi, H. A., 2017a. Minimum requirements for predictive pore-network modelling of solute transport in micromodels. Advances in Water Resources 108, 83–98.

Mehmani, Y., Tchelepi H., 2017b. PNM vs. DNS Intercomparison Dataset for Transport in Micromodels. Digital Rocks Portal. Retrieved March 28, from www.digitalrocksportal.org.

National Research Council, 2005. Contaminants in the Subsurface: Source Zone Assessment and Remediation. Washington, DC: The National Academies Press.

Nilsson, M. A., Kulkarni, R., Gerberich, L., Hammond, R., Singh, R., Baumhoff, E., Rothsetin, J. P., 2013. Effect of fluid rheology on enhanced oil recovery in a microfluidic sandstone device. Journal of Non-Newtonian Fluid Mechanics 202, 112–119.

O'Keefe, Ch. M., Giammanco, D., Li, S., Pisanic II, T. R. P., Wang, T.-H. J., 2019. Multilayer microfluidic array for highly efficient sample loading and digital melt analysis of DNA methylation. Lab on a Chip 19, 444–451.

Orgogozo, L., Golfier, F., Buès, M. A., Quintard, M., Koné, T., 2013. A dual-porosity theory for solute transport in biofilm-coated porous media. Advances in Water Resources 62, 266–279.

Olsson, E., Kreiss, G., 2005. A conservative level set method for two phase Flow, Journal of Computational Physics 210, 225–246.

Papatzakos, P., 2016. A model for multiphase multicomponent, and thermal flow in neutrally wetting porous media, built on the diffuse-interface assumption. Journal of Petroleum Science and Engineering 143, 141–157.

Patel, H. V., Kuipers, J. A. M., Peters, E. A. J. F., 2019. Effect of flow and fluid properties on the mobility of multiphase flows through porous media. Chemical Engineering Science 193, 243–254.

Pesavento, F., Schrefler, B. A., Sciumè, G., 2017. Multiphase Flow in Deforming Porous Media: A Review. Archives of Computational Methods in Engineering 24, 423–448.

Rabbani, H. S., Joekar-Niasar, V., Pak, T., Shokri, N., 2017. New insights on the complex dynamics of two-phase flow in porous media under intermediatewet conditions. Scientific reports 7, 4584.

Renardi, M., Renardy, Y., Li, J., 2001. Numerical Simulation of Moving Contact Line Problems Using a Volume-of-Fluid Method. Journal of Computational Physics 171, 243–263.

Rodríguez de Castro, A., Goyeau, B., 2021. A pore network modelling approach to investigate the interplay between local and Darcy viscosities during the flow of shear-thinning fluids in porous media. Journal of Colloid and Interface Science 590, 446 – 457.

Rodríguez de Castro, A., Ahmadi-Sénichault, A., Omari, A., Savin, S., Madariaga, L.-F., 2016a. Characterizing porous media with the yield stress fluids porosimetry method. Transport in Porous Media 114(1), 213–233.

Rodríguez de Castro, A., Oostrom, M., Shokri, N., 2016b. Effects of shear-thinning fluids on residual oil formation in microfluidic pore networks. Journal of Colloid and Interface Science 472, 34 – 43.

Rodríguez de Castro, A., Shokri, N., Karadimitriou, N., Oostrom, M. and Joekar-Niasar, V., 2015. Experimental study on nonmonotonicity of capillary desaturation curves in a 2-D pore network. Water Resources Research 51, 8517 – 8528.

Romanò, F., Fujioka, H., Muradoglu, M., Grotberg, J. B., 2019. Liquid plug formation in an airway closure model. Physical Review Fluids 4(9).

Romanò, F., Muradoglu, M., Fujioka, H., Grotberg, J. B., 2021. The effect of viscoelasticity in an airway closure model. Journal of Fluid Mechanics, 913.

Saffman, P. G., Taylor, G. I., 1958. The penetration of a fluid into a porousmedium Hele–Shaw cell containing a more viscous liquid, Proceedings of the Royal Society of London A 245 (1958) 312.

Santos, D. S., Faia, P. M., Garcia, F. A. P., Rasteiro, M. G., 2019. Oil/water stratified flow in a horizontal pipe: Simulated and experimental studies using EIT. Journal of Petroleum Science and Engineering 174, 1179–1193.

Schenk, O., Gärtner, K., 2004. Solving unsymmetric sparse systems of linear equations with PARDISO. Future Generation Computer Systems 20, 475–487.

Shende, T., Niasar, V., Babaei, M., 2021a. Upscaling non-Newtonian rheological fluid properties from pore-scale to Darcy' scale. Chemical Engineering Science, 239, 116638.

Shende, T., Niasar, V., Babaei, M., 2021b. Pore-scale simulation of viscous instability for non-Newtonian two-phase flow in porous media. Journal of Non-Newtonian Fluid Mechanics, 296, 104628.

Shende, T., Niasar, V. J., Babaei, M., 2021c. An empirical equation for shear viscosity of shear thickening fluids, J. Mol. Liq. 325, 115220.

Shi, Y., Tang, G. H., 2016. Non-Newtonian rheology property for two-phase Flow on fingering phenomenon in porous media using the lattice Boltzmann method. Journal of Non-Newtonian Fluid Mechanics 229 (2016) 86–95.

Silva, J. A. K., Smith, M. M., Munakata-Marr, J., McCray, J. E., 2012. The effect of system variables on in situ sweep-efficiency improvements via viscosity modification. Journal of Contaminant Hydrology 136–137, 117 – 130.

Sinha, S., Bender, A. T., Danczyk, M., Keepseagle. K., Prather, C. A., Bray, J. M., Thrane, L. W., Seymour, J. D., Codd, S. L., Hansen, A., 2017. Effective Rheology of Two-Phase Flow in Three-Dimensional Porous Media: Experiment and Simulation. Transport in Porous Media 119, 77–94.

Smith, M. M., Silva, J. A. K., Munakata-Marr, J., McCray, J. E., 2008.Compatibility of Polymers and Chemical Oxidants for Enhanced Groundwater Remediation. Environmental Science & Technology, 42(24), 9296–9301.

Sorbie, K.S.: Polymer-Improved Oil Recovery. Blackie and Son Ltd, Glasgow (1991).

Speight, J. G. Chapter 8 - Nonthermal Methods of Recovery, Editor(s): James G. Speight, Introduction to Enhanced Recovery Methods for Heavy Oil and Tar Sands (Second Edition), Gulf Professional Publishing, 2016, Pages 353-403, ISBN 9780128499061.

Stute, B., Krupp, V., von Lieres, E., 2003. Performance of iterative equation solvers for mass transfer problems in three-dimensional sphere packings in COMSOL. imulation Modelling Practice and Theory 33, 115–131.

Tassi, L., Chapter 5 – kinematic viscosity and viscous flow in binary mixtures containing ethane-1,2-diol, in: N.P. Cheremisinoff (Ed.), Advances in Engineering Fluid Mechanics: Multiphase Reactor and Polymerization System Hydrodynamics, Gulf Professional Publishing, Burlington, 1996, pp. 79–104.

Tran, M., Jha, B., 2020. Coupling between transport and geomechanics affects spreading and mixing during viscous fingering in deformable aquifers. Advances in Water Resources 136, 103485.

Truex, M., Vermeul, V. R., Adamson, D. T., Oostrom, M., Zhong, L., Mackley, R. D., Fritz, B. G., Horner, J. A., Johnson, T. C., Thomle, J. N., Newcomer, D. R., Johnson, C. D. ,Rysz, M., Wietsma, T. W., Newell, C. J., 2015. Field Test of Enhanced Remedial Amendment Delivery Using a Shear-Thinning Fluid. Groundwater Monitoring & Remediation 35, 34–45.

Tsakiroglou CD, Theodoropoulou M, Karoutsos V, Papanicolaou D, Sygouni V., 2003. Experimental study of the immiscible displacement of shear-thinning fluids in pore networks. Journal of Colloid Interface Science 267, 217–32.

Tsakiroglou, C. D., Theodoropoulou, M. A., Karoutsos, V., Papanicolaou, D., 2005. Determination of the effective transport coefficients of pore networks from transient immiscible and miscible displacement experiments. Water Resources Research 41, W02014.

Tskiroglou C. D., Aggelopoulos, C. A., Tzovolou, D. N., Theodoropoulou, M. A., Avraam, D. G, 2013. Dynamics of surfactant-enhanced oil mobilization and solubilization in porous media: Experiments and numerical modeling. International Journal of Multiphase Flow 55, 11–23.

Wasan, D. T., Nikolov, A. D., 2003. Spreading of nanofluids on soils. Nature 423. 156–159.

Wang, M., Xiong, Y., Liu, L., Peng, G., Zhang, Z., 2019. Lattice Boltzmann Simulation of Immiscible Displacement in Porous Media: Viscous Fingering in a Shear-Thinning Fluid. Transport in Porous Media, 126, 411–429.

Wilkinson, D., 1984. Percolation model of immiscible displacement in the presence of buoyancy forces. Physical review A 30, 520–531.

World Energy Council, 2010. 2010 Survey of Energy Sources. https://www.worldenergy.org/. Accessed 11 Mar. 2021.

Wu, Y. -S., 1990.Theoretical Studies of Non-Newtonian and Newtonian Fluid Flow through Porous Media. PhD thesis. Department of Materials Science and Mineral Engineering University of California and Earth Sciences Division Lawrence Berkeley Laboratory University of California Berkeley, California 94720

Wu, Y.-S., Pruess, K., & Witherspoon, P. A., 1991. Displacement of a Newtonian fluid by a non-Newtonian fluid in a porous medium. Transport in Porous Media, 6(2).

Xie, Ch., Lv, W., Wang, M., 2018. Shear-thinning or shear-thickening fluid for better EOR? — A direct pore-scale study. Journal of Petroleum Science and Engineering 161, 683–691.

Zhong, L., Oostrom, M., Truex, M. J., Vermeul, V. R., Szecsody, J., 2013. Rheological behavior of xanthan gum solution related to shear thinning fluid delivery for subsurface remediation. Journal of Hazardous Materials 244–245, 160–170.

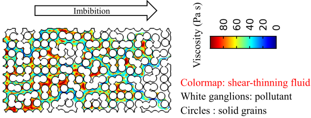
Imbibition
Viscosity (Pa s)
80
60
40
20
0
Colormap: shear-thinning fluid
White ganglions: pollutant
Circles : solid grains